INSTITUTE OF PHYSICS PUBLISHING JOURNAL OF OPTICS A: PURE AND APPLIED OPTICS
J. Opt. A: Pure Appl. Opt. **6** (2004) 289–300 PII: S1464-4258(04)73221-3

Conical diffraction asymptotics: fine structure of Poggendorff rings and axial spike

M V Berry

H H Wills Physics Laboratory, University of Bristol, Tyndall Avenue, Bristol BS8 1TL, UK

Received 3 December 2003, accepted for publication 20 January 2004
Published 10 February 2004
Online at stacks.iop.org/JOptA/6/289 (DOI: 10.1088/1464-4258/6/4/001)

Abstract
The paraxial propagation of a beam incident along an optic axis of a biaxial crystal slab is studied in detail. Analytical descriptions are given for the Poggendorff bright and dark rings (associated with the conical singularity of the dispersion surface), and the axial spike (associated with the toroidal ring in the dispersion surface). The rings and spike depend on distance from the crystal. In sharpest focus, the rings are close and asymmetrical, and the spike is faint. Further away, the rings separate, they develop weak diffraction oscillations, and the spike grows in intensity. Eventually the oscillations disappear and the rings become symmetrical, and the axial spike dominates. The images depend on the profile of the incident beam; explicit formulae are given for a Gaussian beam and a coherently illuminated pinhole. Geometrical optics (extended to complex rays for the Gaussian beam) can describe some aspects of the images, in particular the Poggendorf dark ring, which arises from antifocusing and for which an explicit description is given.

Keywords: diffraction, biaxial, conical interaction, degeneracy, Hamiltonian

1. Introduction

Conical refraction, that is propagation of a beam incident along an optic axis of a slab of biaxial transparent crystal, is perhaps the most singular phenomenon in classical optics, as well as one of the oldest. The basic facts, starting with Hamilton's discovery in the early 1830s, are well known [1, 2]. The beam propagates as a cone, emerging from the crystal as a cylinder. On close examination, the cross section of the cone is seen to consist of two bright rings, separated by a dark ring. These 'Poggendorff rings' arise from the nonzero range of directions of the plane waves into which any spatially localized beam can be decomposed. This is internal conical refraction. However, as emphasized by Raman *et al* [3], the very fact that a range of directions is involved means that external conical refraction is involved too. This originates not from the conical singularity at the optic axis (figure 1) but from the ring singularity (axis of single-ray velocity) of the dispersion surface, and manifests itself as a spike on the symmetry axis of the cone. The distinction between the two phenomena is not sharp: one transforms into the other as the distance from the slab increases. Far away, the rings disappear, and are replaced by the spike.

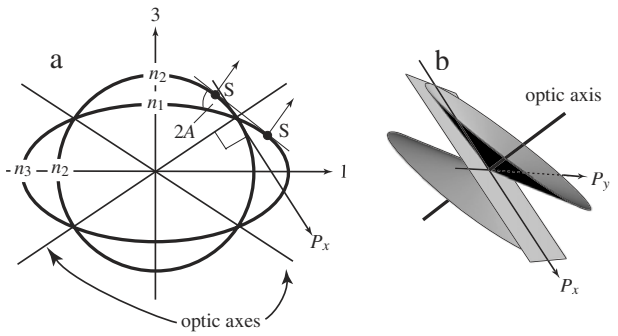

Figure 1. (a) Section of a two-sheeted dispersion surface for a biaxial crystal, showing the optic axes and points S on the circle of single-ray velocity (arrows attached to points S). The surface is a polar plot of refractive indices in the space of wavevector directions; up to magnification, it is a contour (i.e. constant-frequency) plot of the dispersion relation $\omega(\mathbf{k})$; the term wavevector surface is also used [1]. (b) Magnification of conical intersection of sheets near an optic axis, and transverse wavevector coordinates.

Geometrical optics gives an inadequate description. The detailed structure of the rings requires diffraction theory,

formulated in the 1970s by Belskii and Khapaluyk [4, 5] (see also [6], who also confirmed aspects of the theory experimentally). This was further developed by Moskvin *et al* [7], in a detailed study of the asymptotics of the Green function for conical refraction. Additional rings were predicted by Warnick and Arnold [8] but seem not to have been observed yet. The ring structure depends on the profile of the incident beam, an aspect that has been explored recently [9–12].

My aim here is to extend and complement existing theory by providing detailed analytical descriptions of the system of rings and the axial spike, as functions of distance from the slab, in the simplest formulation that captures the different phenomena. This is based on paraxial optics, which can be expressed in terms of Hamiltonian 'evolution' for the wave, with propagation distance playing the role of time (section 2 and the appendix), and the Hamiltonian representing the form of the dispersion surface. The formal solution, giving the wave as a diffraction integral, and essentially reformulating earlier results [4, 5] for completeness, is obtained in section 3.

In section 4, we calculate the 'focal image', that is, the sharpest rings seen with a microscope beyond the crystal focused on a plane inside the crystal (this would be the image plane of the entrance face if the crystal were approximated by an isotropic medium). The ring pattern is asymmetrical, in the sense that the intensity profiles of the two Poggendorff bright rings are different. At increasing distances (section 5), the inner ring acquires oscillations. Eventually these disappear, and the two rings become symmetrical at large distances while broadening and getting fainter. Meanwhile, a maximum appears at the centre of the rings; eventually, this axial spike (section 6) dominates the pattern.

The geometrical optics of conical refraction is discussed in section 7, starting from the Hamiltonian of section 2. This is certainly appropriate, in view of the fact that the prediction of conical refraction by Hamilton was the first nontrivial application of his method. Geometrical optics reproduces the distant bright and dark Poggendorff rings correctly (section 7); as in the usual treatments [2], the dark ring results from a kind of antifocusing. A complex-ray extension of geometrical optics, applicable when the incident beam is Gaussian, gives greater accuracy but still fails to predict the oscillations and asymmetrical form of the rings close to the crystal. The theory also predicts the axial spike, though incorrectly with infinite intensity. The analysis in this section complements earlier mathematical investigations [13–15].

For readers uninterested in the technicalities of the derivations, section 8 contains a summary of the main features of the conical diffraction patterns, and suggestions for experimental investigations.

My emphasis is on a detailed analysis of the simplest case of conical diffraction. There are obvious extensions that I do not explore here. Some have been studied already. For example, if the beam direction is changed so as to no longer lie along an optic axis, conical refraction gives way to double refraction; the transition has been explored for rigid rotation of the crystal relative to the beam [16], and in the generic case where the medium is inhomogeneous as well as anisotropic so that the conical direction can be encountered in the course of propagation [17]. Alternatively, the medium can possess optical activity [18, 19], whose strength is a singular perturbation that destroys the conical singularity. Finally, if the medium possesses absorption (dichroism), its strength is a different singular perturbation, splitting the conical singularity into two 'singular axes' [20, 21]; to my knowledge, the effect of dichroism on conical diffraction has not been investigated.

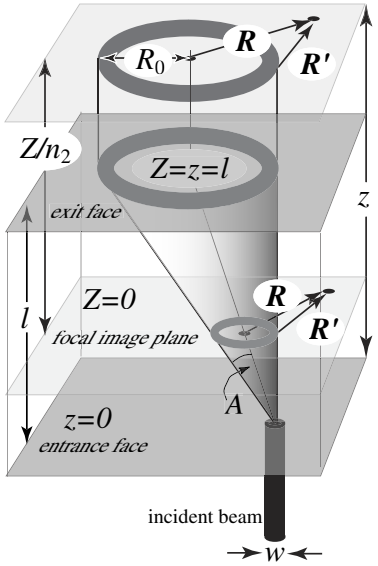

Figure 2. Geometry of crystal slab and incident beam, showing Cartesian coordinates $\mathbf{R}'$, z, with origin on the entrance face, and cone-centred coordinates $\mathbf{R}$, Z, with origin on the focal image plane.

2. Plane waves and Hamiltonian model

We consider a slab of transparent crystal with thickness l and three principal dielectric constants ε_i and refractive indices n_i, satisfying

$$\varepsilon_1 = n_1^2 < \varepsilon_2 = n_2^2 < \varepsilon_3 = n_3^2, \tag{2.1}$$

with small differences between n_1, n_2 and n_3, reflecting paraxiality. We define a crystal wavenumber k in terms of the vacuum wavenumber k_0 by

$$k \equiv n_2 k_0. \tag{2.2}$$

The crystal is cut so that the slab is perpendicular to one of the optic axes, and a beam is incident normally. The resulting refracted light (figure 2) forms a slant cone with the optic axis as one of its generators.

The two plane waves that can travel in the crystal ($0 < z < l$) can be written down almost by inspection, on the basis of a local approximation to the dispersion surface near the conical singularity; a derivation is however outlined in the appendix. Using transverse cone-centred cooordinates $\{x, y, z\} = \{\mathbf{R}, z\}$ (figure 2) and transverse wavevectors $k\mathbf{P} = k\{P_x, P_y\} = kP\{\cos\theta_\mathbf{P}, \sin\theta_\mathbf{P}\}$ (with $P \ll 1$ because of paraxiality), the waves, expressed in terms of the electric displacement vector (which is exactly transverse, unlike the electric field), are

$$\mathbf{D}_{\pm\mathbf{P}}(\mathbf{R}, z) = \exp\{\mathrm{i}k(\mathbf{P}\cdot\mathbf{R} - z(\tfrac{1}{2}P^2 \pm AP))\}\mathbf{d}_\pm(\mathbf{P}). \tag{2.3}$$

Here the orthogonally polarized eigenmodes are

$$\mathbf{d}_+(\mathbf{P}) = \begin{pmatrix} \cos\frac{1}{2}\theta_\mathbf{P} \\ \sin\frac{1}{2}\theta_\mathbf{P} \end{pmatrix}, \qquad \mathbf{d}_-(\mathbf{P}) = \begin{pmatrix} \sin\frac{1}{2}\theta_\mathbf{P} \\ -\cos\frac{1}{2}\theta_\mathbf{P} \end{pmatrix} \tag{2.4}$$

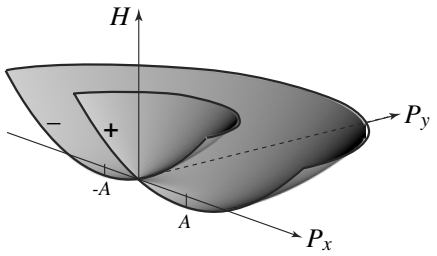

Figure 3. Cutaway showing sheets of the conical Hamiltonian (2.7) for $z < l$.

and

$$A = \frac{1}{n_2}\sqrt{(n_2 - n_1)(n_3 - n_2)}, \tag{2.5}$$

where $\pi/2$-A is the semiangle of the conical intersection of the dispersion surface close to the optic axis, and paraxiality implies the assumption $A \ll 1$ (for aragonite, $A = 0.47°$, and for napthalene, $A = 6.87°$ [3]). Outside the crystal (i.e. $z > l$), these waves (with $k\mathbf{P}$ conserved by symmetry) are given by the same expressions with $A = 0$ and P^2 replaced by $n_2 P^2$ (embodying Snell's law).

The plane waves (2.3) and (2.4) are the evolving (with z) eigenstates of the transverse Hamiltonian

$$\mathsf{H}(\mathbf{P}, z) = \left[\tfrac{1}{2}P^2 1 + AP\begin{pmatrix}\cos\theta_{\mathbf{P}} & \sin\theta_{\mathbf{P}} \\ \sin\theta_{\mathbf{P}} & -\cos\theta_{\mathbf{P}}\end{pmatrix}\right]\Theta(l - z) + \tfrac{1}{2}n_2 P^2 1\Theta(z - l), \tag{2.6}$$

where here and hereafter Θ denotes the unit step. The eigenvalues of this matrix Hamiltonian give the scalar Hamiltonian functions, paraxially representing the two sheets of the dispersion surface, governing propagation of the rays corresponding to the two polarizations:

$$H_\pm(\mathbf{P}, z) = \left[\tfrac{1}{2}P^2 \pm AP\right]\Theta(l - z) + \tfrac{1}{2}n_2 P^2\Theta(z - l). \tag{2.7}$$

These are depicted in figure 3 as surfaces in the space H, $\mathbf{P}$, showing the conical intersection at $\mathbf{P} = 0$, corresponding to the optic axis, and the ring-shaped 'moat' at $P = A$ (where $\nabla H = 0$), corresponding to the axis of single-ray velocity. These features will determine the main features of the geometrical optics (section 7) associated with conical refraction, after we have discussed the diffraction physics, governed by (2.6), in sections 3–6.

Operator (2.6) also describes the evolution (with time) of the quantum state of a spin-1/2 particle in two space dimensions, with the spin coupled to the momentum. This is most immediately seen by writing (2.6) (for $z < l$) as

$$H(\mathbf{P}) = \tfrac{1}{2}P^2 1 + A\mathbf{S}\cdot\mathbf{P} \tag{2.8}$$

where, in terms of the Pauli matrices, $\mathbf{S} = \{\sigma_3, \sigma_1\}$. Therefore, all our subsequent results for the propagation of light beams (e.g. the general solution (3.8)) also describe the evolution of an initial spinor wavepacket. In view of the form of the scalar eigenhamiltonians (2.7) (figure 3), conical diffraction provides an exactly solvable quantum system involving a conical intersection of eigensurfaces.

3. General solution

The wave that evolves from an incident beam with transverse profile $\mathbf{D}(\mathbf{R}, 0)$, having traversed the crystal slab and emerged into the space beyond, can be generated formally by H, regarded as a matrix-valued operator with 'momentum' $\mathbf{P}$ represented by $-\mathrm{i}\nabla_{\mathbf{R}}/k$:

$$\mathbf{D}(\mathbf{R}, z) = \exp\left\{-\mathrm{i}k\int_0^z \mathrm{d}z'\,\mathsf{H}(\mathbf{P}, z')\right\}\mathbf{D}(\mathbf{R}, 0). \tag{3.1}$$

To express this as the familiar superposition of plane waves, we introduce the Fourier transform $\mathbf{a}(\mathbf{P})$ of the incident beam:

$$\mathbf{D}(\mathbf{R}, 0) = \frac{k}{2\pi}\int\int \mathrm{d}\mathbf{P}\,\exp\{\mathrm{i}k\mathbf{P}\cdot\mathbf{R}\}\mathbf{a}(\mathbf{P}). \tag{3.2}$$

Then (3.1) and (2.6) lead to

$$\mathbf{D}(\mathbf{R}, z) = \frac{k}{2\pi}\int\int \mathrm{d}\mathbf{P}\,\exp\left\{\mathrm{i}k\left(\mathbf{P}\cdot\mathbf{R} - \frac{1}{2}ZP^2\right)\right\} \times \left[\cos(kR_0P)1 - \mathrm{i}\sin(kR_0P) \times \begin{pmatrix}\cos\theta_{\mathbf{P}} & \sin\theta_{\mathbf{P}} \\ \sin\theta_{\mathbf{P}} & -\cos\theta_{\mathbf{P}}\end{pmatrix}\right]\mathbf{a}(\mathbf{P}). \tag{3.3}$$

Here we have introduced the notations

$$Z \equiv l + (z - l)n_2, \qquad R_0 \equiv Al, \tag{3.4}$$

in which R_0 is the radius of the cylinder of refraction beyond the crystal (figure 2), and Z measures the distance, in units of n_2, from the focal image plane (this would be the virtual image plane of the entrance face if the crystal were isotropic with index n_2). Thus

$$\begin{aligned} &Z = 0 \quad \text{corresponds to} \quad z = l\left(1 - \frac{1}{n_2}\right) \\ &\qquad\text{(image of entrance face)} \\ &Z = l \quad \text{corresponds to} \quad z = l \quad \text{(exit face)}. \end{aligned} \tag{3.5}$$

For simplicity and convenience, we now assume that the incident beam is uniformly polarized and circularly symmetric, so that

$$\mathbf{D}(\mathbf{R}, 0) = D_0(R)\begin{pmatrix}d_{x0} \\ d_{y0}\end{pmatrix}, \qquad |d_{x0}|^2 + |d_{y0}|^2 = 1. \tag{3.6}$$

Thus

$$\mathbf{a}(\mathbf{P}) = a(P)\begin{pmatrix}d_{x0} \\ d_{y0}\end{pmatrix}, \qquad \text{where}$$

$$a(P) = k\int_0^\infty \mathrm{d}R\,RD_0(R)J_0(kRP), \tag{3.7}$$

where here and hereafter J denotes a Bessel function.

A short calculation now brings wave (3.3) into the form

$$\mathbf{D}(\mathbf{R}, z) = \left[B_0(R, R_0, Z)1 + B_1(R, R_0, Z) \times \begin{pmatrix}\cos\theta_{\mathbf{R}} & \sin\theta_{\mathbf{R}} \\ \sin\theta_{\mathbf{R}} & -\cos\theta_{\mathbf{R}}\end{pmatrix}\right]\begin{pmatrix}d_{x0} \\ d_{y0}\end{pmatrix}, \tag{3.8}$$

where the important functions B_0 and B_1 are defined in terms of

$$\Delta(R, R_0, Z) \equiv \int_0^\infty \mathrm{d}P\,a(P)\exp\left\{-\tfrac{1}{2}\mathrm{i}kZP^2\right\} \times \sin(kR_0P)J_0(kRP) \tag{3.9}$$

by

$$B_0(R, R_0, Z) = \frac{\partial \Delta(R, R_0, Z)}{\partial R_0}$$
$$= k \int_0^\infty \mathrm{d}P\, Pa(P) \exp\left\{-\tfrac{1}{2}\mathrm{i}kZP^2\right\}$$
$$\times \cos(kR_0P) J_0(kRP) \tag{3.10}$$

and

$$B_1(R, R_0, Z) = -\frac{\partial \Delta(R, R_0, Z)}{\partial R}$$
$$= k \int_0^\infty \mathrm{d}P\, Pa(P) \exp\left\{-\tfrac{1}{2}\mathrm{i}kZP^2\right\}$$
$$\times \sin(kR_0P) J_1(kRP). \tag{3.11}$$

Equations (3.8)–(3.11) constitute the exact solution of the paraxial model.

In terms of B_0 and B_1, the light intensity is

$$I(R, z) = \mathbf{D}^*(\mathbf{R}, z) \cdot \mathbf{D}(\mathbf{R}, z)$$
$$= |B_0(R, R_0, Z)|^2 + |B_1(R, R_0, Z)|^2$$
$$+ 2\,\mathrm{Re}[B_0^*(R, Z) B_1(R, Z)]$$
$$\times (\cos\theta_{\mathbf{R}}(|d_{x0}|^2 - |d_{x0}|^2) + 2\sin\theta_{\mathbf{R}}\,\mathrm{Re}[d_{x0}^* d_{y0}]). \tag{3.12}$$

The dependence on the polarization state is simply an azimuthal modulation of the ring pattern. This is an inessential complication here, so we need consider only unpolarized or circularly polarized light, for which the interference between B_0 and B_1 vanishes, and

$$I(R, Z) = |B_0(R, R_0, Z)|^2 + |B_1(R, R_0, Z)|^2. \tag{3.13}$$

This completes the reformulation of the theory of [4, 5].

Two important incident waves, that will be used for some of the subsequent explicit calculations, can be written in terms of a beam width parameter w. Using standard Fourier transforms, these are the Gaussian beam, namely

$$D_0(R) = \exp\left(-\frac{R^2}{2w^2}\right),$$
$$a(P) = kw^2 \exp\left(-\tfrac{1}{2}k^2P^2w^2\right), \tag{3.14}$$

and the beam from a coherently illuminated pinhole, namely

$$D_0(R) = \Theta(w - R), \qquad a(P) = \frac{w}{P} J_1(kPw). \tag{3.15}$$

The structure of the rings will emerge clearly when $R_0 \gg w$, that is for thick slabs.

The following w-scaled variables will be convenient:

$$\rho \equiv \frac{R}{w}, \qquad \rho_0 \equiv \frac{R_0}{w}, \qquad \zeta \equiv \frac{Z}{kw^2}. \tag{3.16}$$

Then, for example, (3.9) becomes, after changing the integration variable to $Q = kwP$,

$$\Delta(R, R_0, Z) \equiv \frac{1}{kw} \int_0^\infty \mathrm{d}Q\, a\left(\frac{Q}{kw}\right) \exp\left\{-\frac{1}{2}\mathrm{i}\zeta Q^2\right\}$$
$$\times \sin(\rho_0 Q) J_0(\rho Q). \tag{3.17}$$

Thick slabs correspond to $\rho_0 \gg 1$.

As illustrations of the phenomena to be explored, figure 4 shows calculations of the light intensity for a Gaussian incident beam. In the focal image $\zeta = 0$ (figure 4(a)), the Poggendorff rings are close together. As ζ increases, the rings separate and become prominent while developing oscillations. Then they get fainter and the axial spike appears, and eventually dominates.

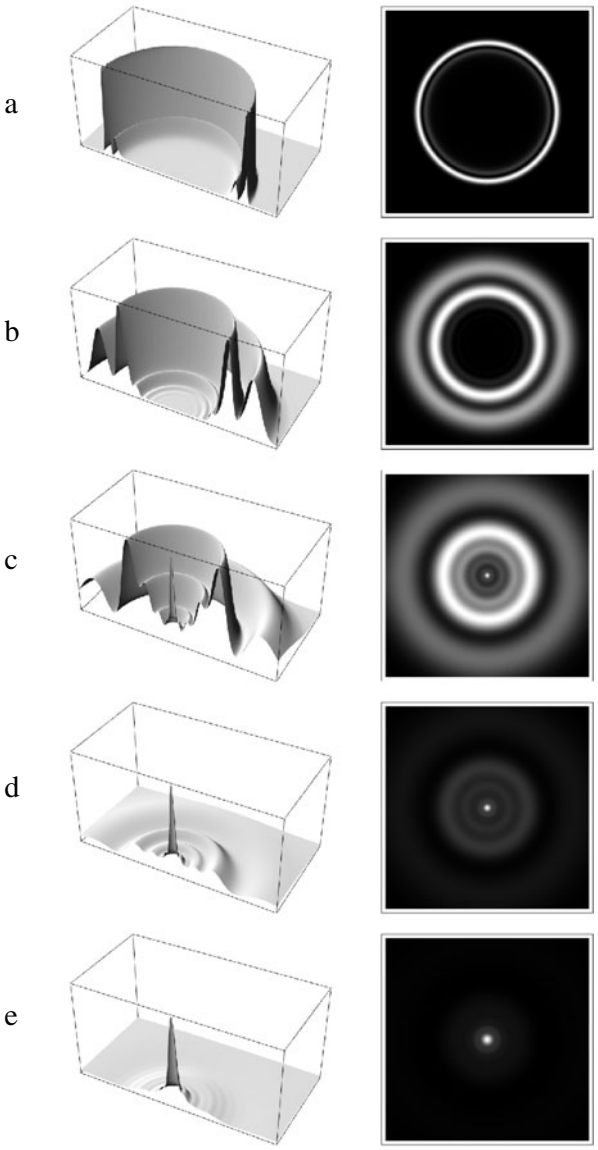

Figure 4. Ring and axial line intensities for a Gaussian incident beam, computed numerically from (3.13); left, cutaway 3D plot; right, density plot for $\rho_0 = 20$ and (a) $\zeta = 0$, (b) $\zeta = 4$, (c) $\zeta = 8$, (d) $\zeta = 10$ and (e) $\zeta = 15$. The coordinate range is $\{-30, 30\}$, that is $\{-1.5R_0, 1.5R_0\}$.

4. Rings in the focal image

Focusing on the plane $Z = \zeta = 0$ with a microscope beyond the slab should give the sharpest image of rings generated by the incident beam. For this case, the fundamental functions B_0 and B_1, defined by (3.10) and (3.11), can be recast in terms of an explicit propagator. First we write (cf (3.9))

$$B_0(R, R_0, 0) = k \int_0^\infty \mathrm{d}R'\, R' D_0(R') \frac{\partial}{\partial R_0} C(R, R', R_0)$$
$$B_1(R, R_0, 0) = -k \int_0^\infty \mathrm{d}R'\, R' D_0(R') \frac{\partial}{\partial R} C(R, R', R_0) \tag{4.1}$$

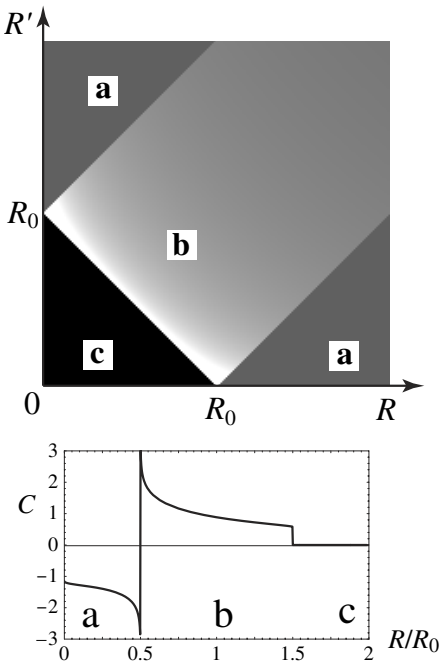

Figure 5. Above: density plot of the 'focusing' propagator C (equation (4.3)), showing the regions a, b and c where the function takes different forms. Below: plot of C for $R'/R_0 = 0.5$.

where

$$C(R, R', R_0) = \int_0^\infty \mathrm{d}P\, J_0(kPR')J_0(kPR)\sin(kPR_0). \tag{4.2}$$

This integral can be evaluated in terms of the complete elliptic integrals K:

$$C(R, R', R_0) = \begin{cases} 0 & (|R-R'| > R_0\text{: region a}) \\ \dfrac{1}{\pi k\sqrt{RR'}} K\left(\dfrac{R_0^2-(R-R')^2}{4RR'}\right) & \\ \qquad (|R-R'| < R_0 < R+R'\text{: region b}) & \\ \dfrac{-2}{\pi k\sqrt{R_0^2-(R-R')^2}} K\left(\dfrac{4RR'}{R_0^2-(R-R')^2}\right) & \\ \qquad (R+R' < R_0\text{: region c}). & \end{cases} \tag{4.3}$$

(We use the notation in Mathematica™ [22].) The geometry of this propagator is shown in figure 5.

It is convenient to describe the profile of the rings using R_0 (that is, the approximate position of the geometrical dark ring) as the origin, so we define

$$X \equiv R - R_0, \qquad \xi \equiv \frac{X}{w}. \tag{4.4}$$

For the thick slabs we are interested in, $|X| \ll R_0$, i.e. $|\xi| \ll \rho_0$. It follows that the derivatives in (3.10) and (3.11) and in (4.1) are approximately equal, so $B_0 \approx B_1$. Another way to see this is to use asymptotic expressions for the Bessel functions in (3.10) and (3.11), whence, up to oscillatory terms that become negligible when integrated,

$$\cos(kR_0P)J_0(kRP) \approx \sin(kR_0P)J_1(kRP) \approx \frac{\cos(kXP-\frac{1}{4}\pi)}{\sqrt{2\pi kR_0P}}. \tag{4.5}$$

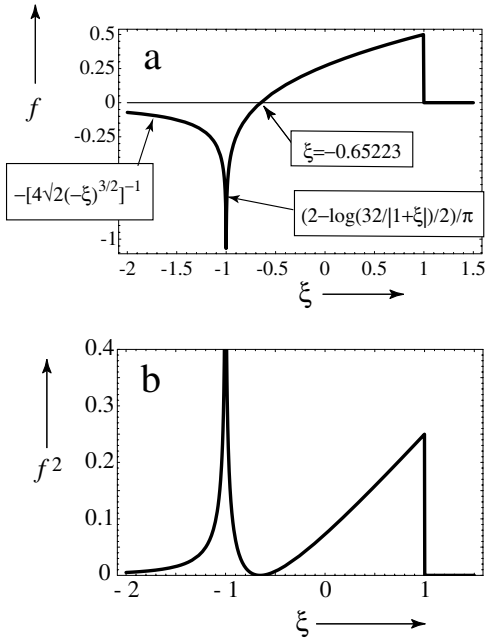

Figure 6. (a) Focused pinhole-beam amplitude (4.8), showing the zero crossing and the asymptotics of the singularity and inner tail. (b) Focused intensity corresponding to (a), showing the two asymmetrical Poggendorff bright rings, with a dark ring between them.

Manipulations of the elliptic integrals K, also involving the elliptic integral E, now bring (4.1)–(4.3) to the convenient form

$$B_0(R, R_0, R, 0) \approx B_1(R, R_0, R, 0) \equiv \frac{1}{\sqrt{\rho_0}} f(\xi), \tag{4.6}$$

where

$$f(\xi) = \tfrac{1}{2}\sqrt{\xi}D_0(w\xi)\Theta(\xi) + \frac{1}{2\pi}\int_{|\xi|}^\infty \mathrm{d}\rho'\, \frac{\rho'^{3/2}}{\rho'^2-\xi^2} D_0(w\rho') \times \left(2E\left(\frac{\rho'-\xi}{2\rho'}\right) - \frac{(\rho'+\xi)}{\rho'}K\left(\frac{\rho'-\xi}{2\rho'}\right)\right) + \frac{\Theta(-\xi)}{\pi\sqrt{2}} \times \int_0^{-\xi} \mathrm{d}\rho' \frac{\rho'}{(\rho'+\xi)\sqrt{\rho'-\xi}} D_0(w\rho')E\left(\frac{2\rho'}{\rho'-\xi}\right). \tag{4.7}$$

For the coherently illuminated pinhole source (3.15), the integrals can be evaluated explicitly, with the result

$$f(\xi) = \begin{cases} 0 & (\xi > 1) \\ \dfrac{1}{\pi}\left(-K\left(\dfrac{1-\xi}{2}\right) + 2E\left(\dfrac{1-\xi}{2}\right)\right) & (|\xi| < 1) \\ \dfrac{\sqrt{2}}{\pi}\left(\sqrt{1-\xi}E\left(\dfrac{2}{1-\xi}\right) + \dfrac{\xi}{\sqrt{1-\xi}}K\left(\dfrac{2}{1-\xi}\right)\right) & \\ \qquad (\xi < -1). & \end{cases} \tag{4.8}$$

Figure 6(a) shows this function, and figure 6(b) shows the intensity f^2. There is a zero at $\xi = -0.652\,23\ldots$ (the Poggendorff dark ring), rising to a step down to zero at $\xi = 1$ (the outer Poggendorff bright ring), and a logarithmic singularity at $\xi = -1$ (the inner Poggendorff bright ring) with

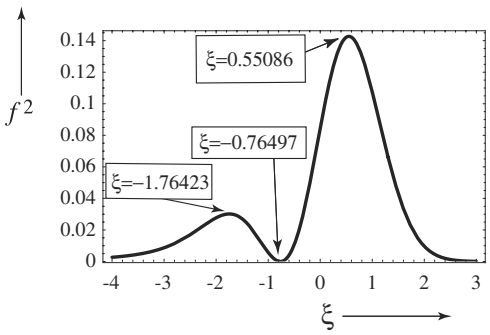

Figure 7. Focused Gaussian-beam intensity (4.10).

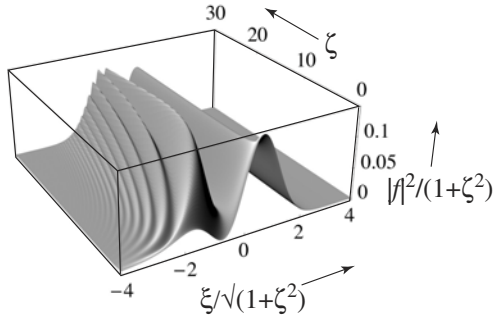

Figure 8. Transition of Poggendorff rings from near to far field for a Gaussian incident beam, calculated from (5.1) and showing the development of oscillations in the inner ring. ξ has been scaled to compensate for the widening of the rings as ζ increases.

an intensity tail decaying as $1/(-\xi)^3$ inwards, that is towards the axis of the ring system. Notwithstanding the singularity, the inner ring contains only 28.79% of the total energy. Belskii and Khapalyuk [5] obtain and describe expressions equivalent to (4.8), expressed in terms of the less familiar Legendre P and Q functions of order $1/2$ and hypergeometric functions of two variables.

For the Gaussian beam (3.14), it is more convenient to evaluate the focused ring profile from the Fourier representation, for which (3.9)–(3.11) and (4.6), with approximation (4.5), give

$$f(\xi)=\frac{1}{\sqrt{2\pi}}\int_0^\infty \mathrm{d}Q\,\sqrt{Q}\exp\left(-\frac{1}{2}Q^2\right)\cos\left(Q\xi-\frac{1}{4}\pi\right). \tag{4.9}$$

This integral can be evaluated in several equivalent forms convenient for numerical calculation. Three such forms, involving the Bessel functions I (not to be confused with the intensity in (3.12)) and K, the parabolic cylinder (Weber) functions D (not to be confused with the beam profile D_0 in (3.6)) and the confluent hypergeometric functions ${}_1F_1$ [23], are

$$\begin{aligned}f(\xi)&=\frac{1}{4\sqrt{2\pi}}|\xi|^{3/2}\exp\left(-\frac{1}{4}\xi^2\right)\Big[K_{\frac{3}{4}}\left(\tfrac{1}{4}\xi^2\right)\\&\quad+\operatorname{sgn}(\xi)K_{\frac{1}{4}}\left(\tfrac{1}{4}\xi^2\right)\\&\quad+\pi\sqrt{2}\Theta(-\xi)\left(I_{\frac{3}{4}}\left(\tfrac{1}{4}\xi^2\right)-I_{\frac{1}{4}}\left(\tfrac{1}{4}\xi^2\right)\right)\Big]\\&=\tfrac{1}{2}\exp\left(-\tfrac{1}{4}\xi^2\right)\big[D_{\frac{1}{2}}(\xi)\Theta(\xi)\\&\quad+\left(\mathrm{i}D_{\frac{1}{2}}(-\xi)+\tfrac{1}{2}(1-\mathrm{i})D_{-\frac{3}{2}}(-\mathrm{i}\xi)\right)\Theta(-\xi)\big]\\&=\frac{1}{4\sqrt{\pi}}\Big(2^{3/4}\Gamma\left(\frac{3}{4}\right){}_1F_1\left(\frac{3}{4},\frac{1}{2},-\frac{1}{2}\xi^2\right)\\&\quad+2^{-3/4}\Gamma\left(\tfrac{1}{4}\right)\xi\,{}_1F_1\left(\tfrac{5}{4},\tfrac{3}{2},-\tfrac{1}{2}\xi^2\right)\Big].\end{aligned} \tag{4.10}$$

The expressions involving I, K and D are analytic, but continuations to $\xi\to\xi\exp(\mathrm{i}\pi)$ are indicated explicitly by the functions sgn and Θ. The expression involving D was derived and discussed by Belsky and Stepanov [9], who also consider thin slabs, for which ρ_0 is not large, so the rings are less distinct.

Figure 7 shows the intensity f^2. Again, the Poggendorff rings are asymmetrical; as with the pinhole beam, the inner ring is the fainter, this time containing 20.24% of the total energy.

5. Transition to rings in the far field

Formula (4.10) describes the focal image $Z=\zeta=0$ for the Gaussian incident beam. It is easy to extend the validity of (4.10) to nonzero Z (in (3.10) and (3.11)), and nonzero ζ (in (3.17)). All that is required is to make the arguments of the exponentials complex, replacing $1/w^2$ by $1/w^2+\mathrm{i}kZ$. Thus (4.10) becomes, for finite ζ, after using (4.6),

$$\begin{aligned}&B_0(R,R_0,Z)\\&\quad\approx B_1(R,R_0,Z)\approx\frac{1}{\sqrt{\rho_0}(1+\mathrm{i}\zeta)^{3/4}}f\left(\frac{\xi}{\sqrt{1+\mathrm{i}\zeta}}\right).\end{aligned} \tag{5.1}$$

Figure 8 shows how the rings evolve away from the focal image $\zeta=0$. The inner ring ($\xi<0$) develops the oscillations discovered by Warnick and Arnold [8]; they derived a formula equivalent to (5.1), in which $f(\xi)$ of (4.10) is expressed in yet another form, involving associated Laguerre functions of fractional order and degree. The rings get wider as ζ increases. For $\zeta>\rho_0$ the width of the rings exceeds their radius, and approximation (5.1) must break down. We do not examine this case, but instead illustrate (figure 9) the high accuracy of (5.1) for $\rho_0\gg1$, by comparing this approximate formula with the exact intensity calculated from (3.10), (3.11) and (3.13).

The additional oscillations in figures 8 and 9 can be described analytically, starting from (5.1) and (4.10) and (for example) using the asymptotics of the Bessel functions K and I to describe the rings for $|\xi|>\sqrt{\zeta}$. For $\xi>0$, the functions K decay exponentially, and there are no oscillations. The exponential decay is still present for $\xi<0$, but each of the exponentially growing additional I Bessel functions, after multiplication by the exponentially decaying prefactor in (4.10), would give a contribution growing as $\sqrt{(-\xi)}$; however, the leading contributions from the two I functions cancel, leaving a net contribution, of order $1/(-\xi)^{3/2}$, from the first correction terms in the Bessel asymptotic expansions. The oscillations result from the interference of this net contribution for the I Bessel functions with the decaying exponential from the K Bessel functions. The formula embodying these considerations is

$$\begin{aligned}\frac{1}{(1+\mathrm{i}\zeta)^{3/4}}f\left(\frac{\xi}{\sqrt{1+\mathrm{i}\zeta}}\right)&\approx\frac{1}{2}\Big[\frac{|\xi|^{1/2}\mathrm{i}^{\Theta(-\xi)}}{(1+\mathrm{i}\zeta)}\\&\quad\times\exp\left(-\frac{\xi^2}{2(1+\mathrm{i}\zeta)}\right)-\frac{\Theta(-\xi)}{|\xi|^{3/2}\sqrt{2}}\Big]\\&\quad(\zeta\gg1,|\xi|>\sqrt{\zeta}).\end{aligned} \tag{5.2}$$

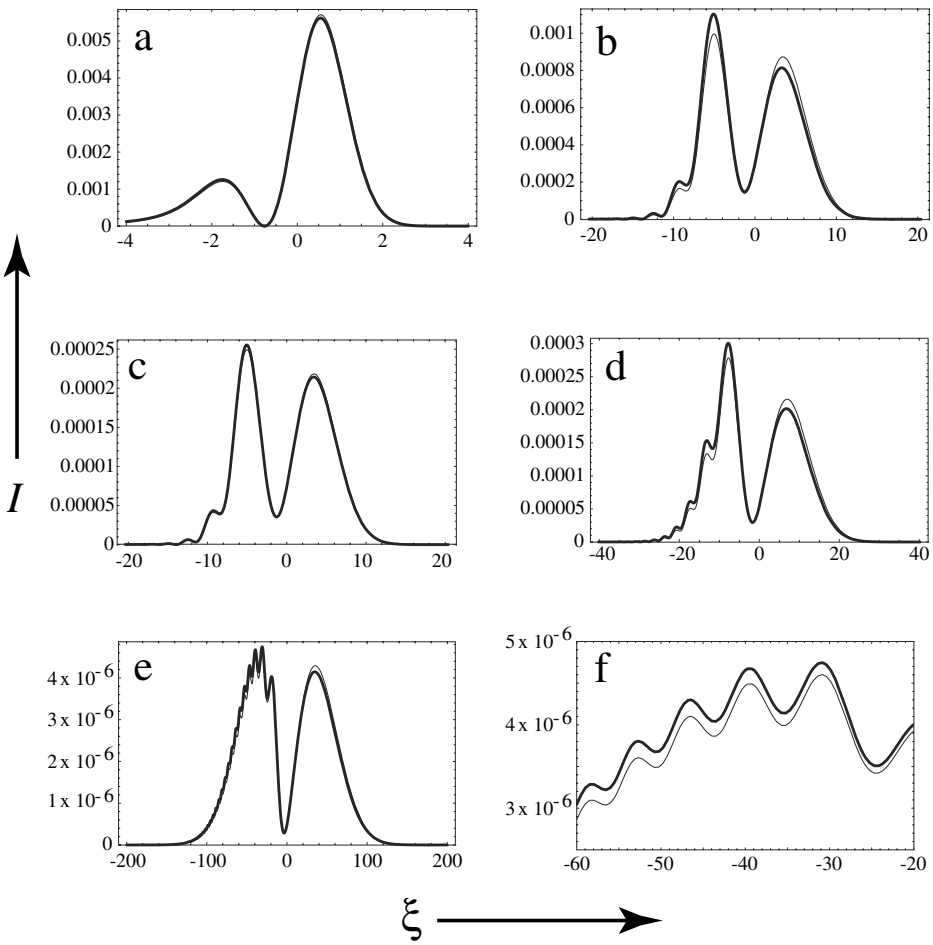

Figure 9. Gaussian-beam ring intensities, calculated from the exact formula (3.13) (thick) and approximation (5.1) (thin). (a) $\zeta = 0$, $\tilde{\rho} = 50$; (b) $\zeta = 5$, $\tilde{\rho} = 50$; (c) $\zeta = 5$, $\tilde{\rho} = 200$; (d) $\zeta = 10$, $\tilde{\rho} = 100$; (e) $\zeta = 50$, $\tilde{\rho} = 1000$; (f) magnification of oscillations decorating the inner ring in (e).

The same result can be derived using (4.9) and (5.1): the first term in (5.2) comes from the saddle-point of the Q integral, and the second term comes from the endpoint $Q = 0$—that is, from the conical point $\mathbf{P} = 0$.

The oscillations have period $\Delta\xi \sim 1$, and so as z increases they get faster in comparison with the thickness ($\sim\zeta$) of the rings. They also get weaker in comparison with the nonoscillatory contributions, so they fade away when $\zeta \gg 1$, leading to the symmetric asymptotic ring pattern (figure 10(a))

$$I(R, Z) \approx \frac{2}{\rho_0(1+\zeta^2)^{3/4}}\left|f\left(\frac{\xi}{1+\mathrm{i}\zeta}\right)\right|^2 \approx \frac{|\xi|}{2\rho_0\zeta^2}\exp\left(-\frac{\xi^2}{\zeta^2}\right) \qquad (\zeta \gg 1, |\xi| > \sqrt{\zeta}). \tag{5.3}$$

The factor $|\xi|$ describes the Poggendorff dark ring.

It is worth pointing out the unusual asymptotic phenomenon represented by this result. The main contribution comes from the subdominant exponential, because the leading-order contributions from the dominant exponentials cancel, leaving the correction to the dominant exponential, which is small in the region of physical interest.

This formula for the asymptotic rings for a Gaussian beam can be generalized to any incident beam. When Z is large, the integrals over P in (3.10) and (3.11) can be evaluated by the stationary phase method, after making the large-ρ_0 approximation (4.5), treating the factor $a(P)$ as slowly varying. The result, incorporating (3.13), is

$$I(R, Z) \approx \frac{|R - R_0|}{2R_0Z^2}\left|a\left(\frac{R - R_0}{Z}\right)\right|^2 = \frac{|X|}{2R_0Z^2}\left|a\left(\frac{X}{Z}\right)\right|^2. \tag{5.4}$$

Again, the zero of the factor $|X|$ gives the Poggendorff dark ring.

For pinhole beam (3.15), (5.4) gives

$$I(R, Z) \approx \frac{1}{2\rho_0|\xi|}\left(J_1\left(\frac{\xi}{\zeta}\right)\right)^2, \tag{5.5}$$

as illustrated in figure 10(b).

6. Axial spike

On the axis $R = \rho = 0$, the integral B_1 (equation (3.11)) vanishes, and the integral B_0 (equation (3.10)) can be evaluated exactly for the Gaussian beam (3.14), with the result

$$B_0(0, R_0, Z) = \frac{1}{1+\mathrm{i}\zeta}\left[1 + \mathrm{i}\rho_0\sqrt{\frac{\pi}{2(1+\mathrm{i}\zeta)}} \times \exp\left(-\frac{\rho_0^2}{2(1+\mathrm{i}\zeta)}\right)\mathrm{erf}\left(\frac{\mathrm{i}\rho_0}{\sqrt{2(1+\mathrm{i}\zeta)}}\right)\right]. \tag{6.1}$$

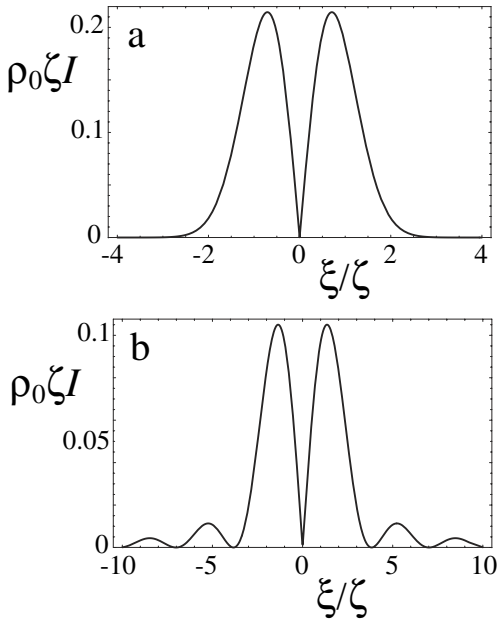

Figure 10. (a) Asymptotic (i.e. $\zeta \gg 1$) Gaussian-beam ring intensity $\rho_0\zeta I$, calculated from (5.3). (b) Asymptotic (i.e. $\zeta \gg 1$) pinhole-beam ring intensity $\rho_0\zeta I$, calculated from (5.5).

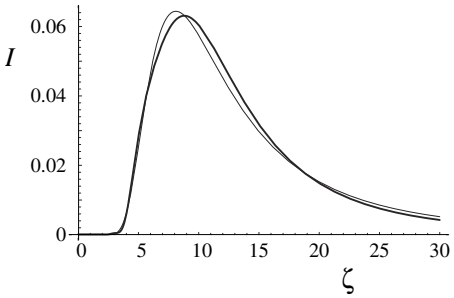

Figure 11. Axial intensity ($\rho = 0$) for Gaussian incident beam, from exact formula (6.1) (thick) and approximation (6.3) (thin), for $\tilde{\rho} = 10$.

Figure 11 shows the axial intensity increasing from very small values (of order $1/\rho_0^4$ at $z = 0$) to a maximum, and then slowly decaying.

For the case $\rho_0 \gg 1$ that we are interested in, we can use the asymptotic approximation for the error function of complex argument. As in the last section, there are large and small exponentials; including both gives

$$B_0(0, R_0, Z) \approx \sqrt{\frac{\pi}{2}}\frac{\mathrm{i}\rho_0}{(1+\mathrm{i}\zeta)^{3/2}}\exp\left(-\frac{\rho_0^2}{2(1+\mathrm{i}\zeta)}\right) - \frac{1}{\rho_0^2}. \tag{6.2}$$

The first term comes from the subdominant contribution (lower limit of the Gaussian integral representing erf), and the second term $1/\rho_0^2$ comes from the first correction to the dominant exponential (upper limit of the integral). Again, we have the paradoxical situation that in the region of interest the subdominant exponential gives the greater contribution. Moreover, we can replace $1+\mathrm{i}\zeta$ by $\mathrm{i}\zeta$ (even for $\zeta \ll 1$, because B_0 is small in this case), giving, for the intensity (3.13),

$$I(R, Z) \approx \frac{\pi\rho_0^2}{2\zeta^3}\exp\left(-\frac{\rho_0^2}{\zeta^2}\right). \tag{6.3}$$

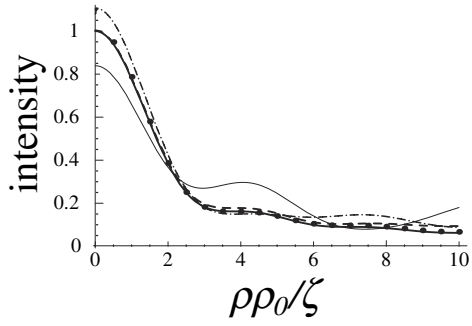

Figure 12. Axial spike intensity profiles for Gaussian incident beam, calculated from the Bessel approximation (6.5) (thick), and exactly from (3.13) for $\tilde{\rho} = 20$: $\zeta = 15$ (thin), $\zeta = 17$ (chain), $\zeta = 20$ (dashed), $\zeta = 30$ (dots). The quantity plotted (cf (6.5) and (3.14)) is $[2\zeta^3\exp(\rho_0^2/\zeta^2)/\pi\rho_0^2]I$.

Thus for a ring of radius ρ_0 the axial intensity is greatest for $\zeta = \rho_0\sqrt{2}$. Figure 11 shows that this approximation is very accurate.

Once again, the large-ρ_0 approximation can be generalized to any incident beam. Using the stationary phase method to evaluate integral (3.10), treating $a(P)$ as slowly varying, gives

$$I(0, Z) \approx \frac{\pi k R_0^2}{2Z^3}\left|a\left(\frac{R_0}{Z}\right)\right|^2. \tag{6.4}$$

A slight extension of this argument gives the form of the axial spike away from the axis. Provided $R \ll R_0$, i.e. $\rho \ll \rho_0$, the Bessel functions can be included in the slowly varying part of the integrands in (3.10) and (3.11). The result, expressed in terms of the dimensionless variables, is

$$I(R, Z) \approx \frac{\pi\rho_0^2}{2k^2w^4\zeta^3}\left|a\left(\frac{\rho_0}{kw\zeta}\right)\right|^2 \times\left[\left(J_0\left(\frac{\rho\rho_0}{\zeta}\right)\right)^2 + \left(J_1\left(\frac{\rho\rho_0}{\zeta}\right)\right)^2\right]. \tag{6.5}$$

As illustrated in figure 12 for the Gaussian beam, this formula gives a good description of the axial spike, with accuracy increasing with ζ.

7. Geometrical optics

The ray Hamiltonians $H_\pm$ given by (2.7) do not depend on the transverse position $\mathbf{R}$, so $\mathbf{P}$ is conserved and can, together with the initial position $\mathbf{R}_\mathrm{i}$, be used to label ray trajectories $\mathbf{R}_\pm(z)$. These are determined by the Hamilton equation

$$\frac{\mathrm{d}\mathbf{R}_\pm}{\mathrm{d}z} = \nabla_\mathbf{P} H_\pm = (\mathbf{P} \pm \mathbf{e}_\mathbf{P})\Theta(l - z) + n_2\mathbf{P}\Theta(z - l),$$
$$\mathbf{e}_\mathbf{P} = \frac{\mathbf{P}}{P}, \tag{7.1}$$

representing ray directions as normals to the surfaces in figure 3. Outside the crystal, the solution, using the coordinate Z defined by (3.4), is

$$\mathbf{R}_\pm(z) = \mathbf{R}_\mathrm{i} + Z\mathbf{P} \pm R_0\mathbf{e}_\mathbf{P}. \tag{7.2}$$

Solving for the momentum $\mathbf{P}$ of the ray reaching $\mathbf{R}$ from the initial position $\mathbf{R}_\mathrm{i}$ gives

$$\mathbf{P}_\pm = \alpha_\pm\mathbf{e}_{\mathbf{R}-\mathbf{R}_\mathrm{i}}, \tag{7.3}$$

where the possible values of α are

$$\alpha_+ = \frac{|\mathbf{R}-\mathbf{R}_\mathrm{i}| - R_0}{Z} \qquad (\text{if } |\mathbf{R}-\mathbf{R}_\mathrm{i}| > R_0)$$
$$\alpha_- = \frac{|\mathbf{R}-\mathbf{R}_\mathrm{i}| + R_0}{Z} \quad \text{and} \quad \frac{|\mathbf{R}-\mathbf{R}_\mathrm{i}| - R_0}{Z} \qquad (7.4)$$
$$(\text{if } |\mathbf{R}-\mathbf{R}_\mathrm{i}| < R_0).$$

Figure 13 illustrates the geometrical origin of these rays from the + and − sheets of the Hamiltonian (dispersion surface) (2.7) (figure 3): one from each sheet when $|\mathbf{R}-\mathbf{R}_\mathrm{i}| > R_0$, and both from the − sheet when $|\mathbf{R}-\mathbf{R}_\mathrm{i}| < R_0$.

The intensity of the ring pattern in geometrical optics, at position $\mathbf{R}$ in the plane Z, is given by the density of those rays in the incident beam that reach $\mathbf{R}, Z$. Consider first the far field, where the spreading of the rays is governed by the momentum distribution $|a(\mathbf{P})|^2$ in the incident beam, which we can take to be localized in position at $\mathbf{R}_\mathrm{i} = 0$. Thus the intensities from the + and − ray families are

$$I_{\pm\mathrm{geom}}(\mathbf{R}, Z) = \frac{1}{2}|a(P_\pm)|^2 \left|\det \frac{\mathrm{d}\mathbf{R}_\pm}{\mathrm{d}\mathbf{P}}\right|^{-1}, \qquad (7.5)$$

where the factor $1/2$ incorporates the equal division between the two polarizations + and −, assuming unpolarized incident light. Differentiating the trajectory (7.2) gives

$$\left(\det \frac{\mathrm{d}\mathbf{R}_\pm}{\mathrm{d}\mathbf{P}}\right) = \det \begin{pmatrix} Z \pm R_0 \frac{P_y^2}{P^3} & \mp R_0 \frac{P_x P_y}{P^3} \\ \mp R_0 \frac{P_x P_y}{P^3} & Z \pm R_0 \frac{P_x^2}{P^3} \end{pmatrix}$$
$$= Z\left(Z \pm \frac{R_0}{P}\right), \qquad (7.6)$$

and substituting (7.3) and (7.4) with $\mathbf{R}_\mathrm{i} = 0$ leads to

$$\left|\det \frac{\mathrm{d}\mathbf{R}_+}{\mathrm{d}\mathbf{P}}\right|^{-1} = \frac{|R-R_0|}{Z^2 R}\Theta(R-R_0)$$
$$\left|\det \frac{\mathrm{d}\mathbf{R}_-}{\mathrm{d}\mathbf{P}}\right|^{-1} = \frac{(R+R_0)}{Z^2 R} + \frac{|R-R_0|\Theta(R_0-R)}{Z^2 R}. \qquad (7.7)$$

Finally, adding the + and − contributions gives

$$I_\mathrm{geom}(R, Z) = \frac{1}{2Z^2 R}\left(|R-R_0|\left|a\left(\frac{|R-R_0|}{Z}\right)\right|^2 + (R+R_0)\left|a\left(\frac{R+R_0}{Z}\right)\right|^2\right). \qquad (7.8)$$

Now we examine the implications of this formula, starting with the rings, where $R \sim R_0$. Since the argument of a in the second term ($\sim 2R_0/Z$) lies outside the angular range of the beam in all cases of interest, this term is negligible. Therefore, the main contribution comes from the first term, which correctly reproduces the asymptotic rings formula (5.4). It is clear that the Poggendorff dark ring originates in the zero of the factor $|R-R_0|$ in the first equation in (7.7) for the Jacobian factor in the intensity. This explanation, implicit in the usual treatments [2], associates the dark ring with a kind of antifocusing arising from the conical singularity: the measure of the region associated with the contributing rays vanishes at the conical point.

It is tempting to interpret the oscillations in the diffractive intensity of the rings, as captured by (5.3) (see figures 8 and 9), in terms of interference between the two rays whose intensities are the terms in (7.8). But this is wrong, because the polarization states (cf (2.4)) associated with the two rays (7.4) (figure 13) are orthogonal and so cannot interfere. The reasons for the orthogonality are different for $R > R_0$ and $R < R_0$: for $R > R_0$, the two rays originate on different sheets, with momenta $\mathbf{P}$ with the same azimuths $\theta_\mathbf{P}$; for $R < R_0$, the rays originate on the same sheet, but with opposite momenta, i.e. $\theta_\mathbf{P}$ and $\theta_\mathbf{P} + \pi$. The true source of the oscillations is interference between the main contributing geometric ray and a 'diffracted ray' from the cone (see the remarks following (5.2)).

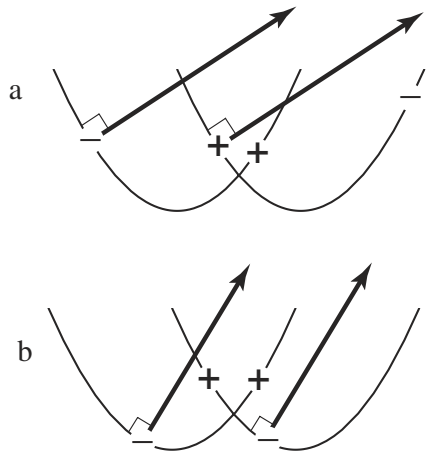

Figure 13. Solutions of ray slope equations (7.4) (normals to Hamiltonian of figure 3). (a) $|\mathbf{R}-\mathbf{R}_\mathrm{i}| > R_0$; (b) $|\mathbf{R}-\mathbf{R}_\mathrm{i}| < R_0$.

Consider now the axial spike, for which $R \sim 0$ and the two terms in (7.8) are almost equal. Thus geometrical optics predicts the spike profile

$$I^{\mathrm{spike}}_\mathrm{geom}(R, Z) \approx \frac{R_0}{Z^2 R}\left|a\left(\frac{R_0}{Z}\right)\right|^2 \qquad (R \approx 0) \qquad (7.9)$$

—apparently contradicting the Bessel profile (6.5), and moreover diverging at $R = 0$. However, the divergence is a focusing effect, arising from the coincidence of all the normals to $H_\pm$ (figure 3) at the ring-shaped 'moat' $P = A$ (axis of single-ray velocity) where the dispersion surface is locally toroidal. Like all focusing effects, this divergence is softened by diffraction, as described by (6.5). And slightly away from the axis, where $\rho\rho_0/\zeta \gg 1$, that is $R > Z/kR_0$, the asymptotics of the Bessel functions in (6.5) reproduces (7.9) exactly. This situation is closely analogous to the optical glory in light from a raindrop [24–26], in which backward scattering (or, in the quantum analogue [27, 28], forward scattering) is dominated by an axial caustic, whose focal singularity is also softened by diffraction associated with a toroidal wavefront. The mild oscillations in the Bessel profile (6.5) (see figure 12) can be regarded as interference between the ray contributions in (7.8) when R is small, in a higher-order geometrical-optics approximation (the lowest-order interference cancels).

The total energy of the wave at distance Z must of course equal the energy in the incident beam (reflections are neglected in our paraxial treatment). Most of this energy is contained in the rings, as can be seen by integrating the approximate ring profile (5.4) across the $\mathbf{R}$ plane:

$$\frac{1}{2R_0Z^2}\int\int_{\mathbf{R}\ \text{plane}} \mathrm{d}\mathbf{R}\,|R-R_0|\left|a\left(\frac{R-R_0}{Z}\right)\right|^2$$
$$\approx \frac{2\pi R_0}{2R_0Z^2}\int_{-\infty}^{\infty}\mathrm{d}X\,|X|\left|a\left(\frac{X}{Z}\right)\right|^2$$
$$= 2\pi\int_0^{\infty}\mathrm{d}P\,|P||a(P)|^2 = \int\int_{\mathbf{R}\ \text{plane}}\mathrm{d}\mathbf{R}\,|D_0(\mathbf{R})|^2. \tag{7.10}$$

Now recall that (5.4) is a local approximation to the first term in the exact geometrical-optics formula (7.8). Integration of (7.8) across the $\mathbf{R}$ plane without the approximation leading to (5.4) shows that the energy is distributed between the two terms in (7.8) in a way that is not obvious:

$$\int\int \mathrm{d}\mathbf{R}\,I_{\mathrm{geom}}(R,Z)$$
$$= \frac{\pi}{Z^2}\left[\int_0^{\infty}\mathrm{d}X\,X\left|a\left(\frac{X}{Z}\right)\right|^2 + \int_0^{R_0}\mathrm{d}X\,X\left|a\left(\frac{X}{Z}\right)\right|^2 + \int_{R_0}^{\infty}\mathrm{d}X\,X\left|a\left(\frac{X}{Z}\right)\right|^2\right]$$
$$= \frac{1}{2}\int\int_{\mathbf{P}\ \text{plane}}\mathrm{d}\mathbf{P}\,|a(\mathbf{P})|^2 + \frac{1}{2}\int\int_{P<R_0/Z}\mathrm{d}\mathbf{P}\,|a(\mathbf{P})|^2 + \frac{1}{2}\int\int_{P>R_0/Z}\mathrm{d}\mathbf{P}\,|a(\mathbf{P})|^2$$
$$= \int\int_{\mathbf{P}\ \text{plane}}\mathrm{d}\mathbf{P}\,|a(\mathbf{P})|^2 = \int\int_{\mathbf{R}\ \text{plane}}\mathrm{d}\mathbf{R}\,|D_0(\mathbf{R})|^2. \tag{7.11}$$

These considerations suggest that very little energy is contained in the central spike, and indeed estimating the integral of (7.9) over the area $R < R_0$ within the ring gives the spike energy

$$\int\int_{R<R_0}\mathrm{d}\mathbf{R}\,I_{\mathrm{geom}}^{\mathrm{spike}}(R,Z) \sim \frac{2\pi R_0^2}{Z^2}\left|a\left(\frac{R_0}{Z}\right)\right|^2, \tag{7.12}$$

which is small whenever the rings are clearly visible ($R_0 \gg Z/kw$).

The above geometrical theory, in terms of rays issuing from $\mathbf{R}=0$ in different directions, cannot describe the rings for small Z. For this, it is necessary to consider the spatial width w as well as the angular width $1/kw$. For general beams, this would involve propagating the geometrical Wigner distribution function in the phase space $\{\mathbf{R},\mathbf{P}\}$, or, if the beam is incoherent, averaging $\mathbf{R}$ in (7.8) over the beam profile. However, for a coherent Gaussian beam there is a remarkable alternative that gives the exact geometrical limit for any Z.

As is known [29], a freely propagating Gaussian beam with waist width w can be generated from the paraxial propagation of a family of rays that starts from $\mathbf{R}=0$ not at the 'time' $z=0$ but from the complex 'time' $z=\mathrm{i}kw^2$. This can be seen most simply from the geometrical amplitude formula

$$\psi = \text{constant}\times\sqrt{\det\left(\frac{\partial^2 S}{\partial R_i\,\partial R_j}\right)}\exp(\mathrm{i}kS), \tag{7.13}$$

where S is the action $R^2/2z$, by substituting $z\to z-\mathrm{i}kw^2$. The result of applying this procedure to the geometrical intensity is equivalent to replacing Z by $Z\to Z-\mathrm{i}kw^2$ in formula (7.8)

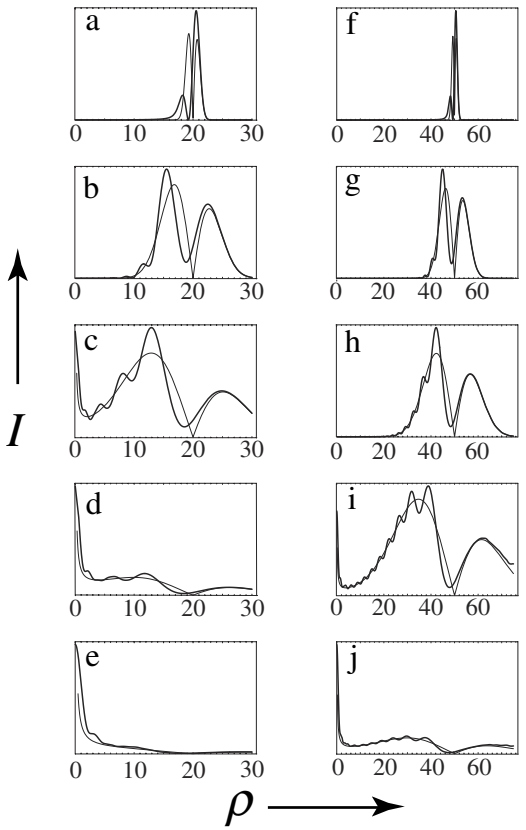

Figure 14. Ring and spike intensities for Gaussian beam, calculated from the exact formula (3.13) (thick) and the complexified ray formula (7.14) (thin), for (a)–(e) $\rho_0=20$ and (f)–(j) $\rho_0=50$, at distances (a) $\zeta=0$, (b) $\zeta=4$, (c) $\zeta=8$, (d) $=10$, (e) $\zeta=15$, (f) $\zeta=0$, (g) $\zeta=5$, (h) $\zeta=10$, (i) $\zeta=18$ and (j) $\zeta=22$.

for the Gaussian beam. (This procedure is the geometrical-optics analogue of the replacement described at the beginning of section 5, which extended diffraction theory from $Z=0$ to finite values of Z—or, more accurately, it is an inverse analogue, since we are now extending geometrical optics from large Z to smaller Z.)

In dimensionless variables, this complex-ray version of geometrical optics gives

$$I_{\mathrm{geom}} = \frac{1}{2(1+\zeta^2)}\left[\frac{(\rho-\rho_0)}{\rho}\exp\left\{-\frac{(\rho-\rho_0)^2}{1+\zeta^2}\right\} + \frac{|\rho+\rho_0|}{\rho}\exp\left\{-\frac{(\rho+\rho_0)^2}{1+\zeta^2}\right\}\right]. \tag{7.14}$$

Figure 14 shows how this formula reproduces the main features of the exact rings and spike, but fails for the following three essentially wave aspects of conical diffraction: for the secondary oscillations, since (7.14) gives only the average over the oscillations; for the finite intensity on the axis, since (7.14) predicts infinite intensity, and for the asymmetrical Poggendorff ring profiles in the focal image $Z=0$ (figure 14(a)).

8. Summary and concluding remarks

The sharpest Poggendorff rings are predicted (section 4) to occur at the focal image $Z=0$, with profiles depending on the

incident beam profile—different, for example, for a coherently illuminated pinhole (4.8) (figure 6) and a Gaussian beam (4.10) (figure 7). It is not easy to resolve the two rings, whose separation is of order w. For example, they are not resolved in the experiments of Raman *et al* [3] with naphthalene. In these experiments, the cited data ($A = 6.87°$, $l \sim 2.5$ mm, $w \sim 1$ μm) give $w/R_0 \sim 1/300$, explaining 'the extreme sharpness of the circular ring...' and the fact that '... it is noteworthy also that the so-called Poggendorff dark circle does not appear in the focal image of the point source...'. More discriminating experiments should enable the two rings to be distinguished, and establish the dependence on beam profile.

Further from the crystal (section 5), the separation of the two rings increases, and is of order $w\sqrt{[1 + (Z/kw^2)^2]}$ (cf (5.1)). Additional rings develop (figures 8 and 9), as described for the Gaussian beam by the exact formula (5.1) with (4.10), or, for large Z, by the simpler formula (5.2). When $Z \gg kw^2$, the oscillations disappear, and the Poggendorff rings (equations (5.3)–(5.5) and figure 10) become symmetrical, with the separation between the two rings growing as Z/kw. This transition, and especially the profile of the rings, should be explored experimentally.

On the axis (section 6), the intensity is small for small Z, but grows rapidly (equations (6.1)–(6.3) and figure 11), rising to a maximum value when $Z \sim kwR_0$, of order $(k/Z)^3(R_0w^2)^2$ (with intensity normalized to unity). The axial spike is especially prominent in the far-from-focus images of Raman *et al* [3]. It is narrow, with width (6.5) being $\Delta R \sim Z/kR_0$. Measurements of its predicted 'Bessel' profile ((6.5) and figure 12) are desirable.

Acknowledgments

I thank Professor J F Nye for many helpful suggestions. My research is supported by the Royal Society.

Appendix. Origin of the wave (2.3)

With Cartesian coordinates $\mathbf{r}' = \{\mathbf{R}', z\}$ (figure 2), a scalar plane wave with wavevector $\mathbf{k}_{\rm tot}$ can be written

$$\exp\{\mathrm{i}\mathbf{k}_{\rm tot}\cdot\mathbf{r}'\} = \exp\left\{\mathrm{i}\left(k\mathbf{P}\cdot\mathbf{R}' + z\sqrt{k_{\rm tot}^2 - k^2P^2}\right)\right\}. \quad \text{(A.1)}$$

In terms of the refractive index $n(\mathbf{P}) \equiv n_2(1 + \mu(\mathbf{P}))$ for propagation in a direction specified by $\mathbf{P}$, and using (2.2),

$$k_{\rm tot} = n(\mathbf{P})k_0 = n_2(1 + \mu(\mathbf{P}))k_0 = (1 + \mu(\mathbf{P}))k. \quad \text{(A.2)}$$

Expanding the exponent in (A.1) to lowest order in μ and P gives the paraxial wave

$$\exp\{\mathrm{i}k(z + \mathbf{P}\cdot\mathbf{R}' - z(\tfrac{1}{2}P^2 - \mu(\mathbf{P})))\}. \quad \text{(A.3)}$$

Near the optic axis $\mathbf{P} = 0$, the dispersion surface is given by a slanted circular cone [2], that with a choice of x axis can be written

$$\mu^{\pm}(\mathbf{P}) = A(P_x \mp P). \quad \text{(A.4)}$$

The scalar parts of the waves (2.3) now follow, after ignoring the irrelevant factor $\exp(\mathrm{i}kz)$ and changing to new transverse coordinates (figure 2)

$$\mathbf{R} = \mathbf{R}' + A\mathbf{e}_x z, \quad \text{(A.5)}$$

whose origin $\mathbf{R} = 0$ corresponds to the axis of the cone of refracted rays. (This argument ignores corrections to (A.4), quadratic in P_x and P_y, because their coefficients are of order $n_2 - n_1$ and $n_3 - n_2$ and therefore negligible compared with the coefficient $1/2$ in (A.3).)

The polarizations of the waves in (2.3) are chosen to be orthogonal and to incorporate the sign change of the eigenvectors around the optic axis [30].

References

[1] Landau L D, Lifshitz E M and Pitaevskii L P 1984 *Electrodynamics of Continuous Media* (Oxford: Pergamon)
[2] Born M and Wolf E 1959 *Principles of Optics* (London: Pergamon)
[3] Raman C V, Rajagopalan V S and Nedungadi T M K 1941 Conical refraction in naphthalene crystals *Proc. Indian Acad. Sci.* A **14** 221–7
[4] Belskii A M and Khapalyuk A P 1978 Propagation of confined light beams along the beam axes (axes of single ray velocity) of biaxial crystals *Opt. Spectrosc.* **44** 312–5
[5] Belskii A M and Khapalyuk A P 1978 Internal conical refraction of bounded light beams in biaxial crystals *Opt. Spectrosc.* **44** 436–9
[6] Schell A J and Bloembergen N 1978 Laser studies of internal conical diffraction. I. Quantitative comparison of experimental and theoretical conical intensity distribution in aragonite *J. Opt. Soc. Am.* **68** 1093–8
[7] Moskvin D N, Romanov V P and Val'kov A Y 1993 Green's function of the electromagnetic field in biaxial media *Phys. Rev.* E **48** 1436–46
[8] Warnick K F and Arnold D V 1997 Secondary dark rings of internal conical refraction *Phys. Rev.* E **55** 6092–6
[9] Belsky A M and Stepanov M A 1999 Internal conical refraction of coherent light beams *Opt. Commun.* **167** 1–5
[10] Belafhal A 2000 Theoretical intensity distribution of internal conical refraction *Opt. Commun.* **178** 257–68
[11] Stepanov M A 2002 Transformation of Bessel beams under internal conical refraction *Opt. Commun.* **212** 11–6
[12] King T A, Hogervorst W, Kazak N S, Khilo N A and Ryzhevich A A 2001 Formation of higher-order Bessel light beams in biaxial crystals *Opt. Commun.* **187** 407–14
[13] Ludwig D 1961 Conical refraction in crystal optics and hydromagnetics *Commun. Pure Appl. Math.* **14** 113–24
[14] Uhlmann G A 1982 Light intensity distribution in conical refraction *Commun. Pure Appl. Math.* **35** 69–80
[15] Melrose R B and Uhlmann G A 1979 Microlocal structure of involutive conical refraction *Duke Math. J.* **46** 571–82
[16] Dreger M A 1999 Optical beam propagation in biaxial crystals *J. Opt. A: Pure Appl. Opt.* **1** 601–16
[17] Naida O N 1979 'Tangential' conical refraction in a three-dimensional inhomogeneous weakly anisotropic medium *Sov. Phys.—JETP* **50** 239–45
[18] Schell A J and Bloembergen N 1978 Laser studies of internal conical diffraction. II. Intensity patterns in an optically active crystal, α-iodic acid *J. Opt. Soc. Am.* **68** 1098–106
[19] Belsky A M and Stepanov M A 2002 Internal conical refraction of light beams in biaxial gyrotropic crystals *Opt. Commun.* **204** 1–6
[20] Ramachandran G N and Ramaseshan S 1961 Crystal optics *Handbuch der Physik* vol XXV/I, ed H Flügge (Berlin: Springer)

[21] Berry M V and Dennis M R 2003 The optical singularities of birefringent dichroic chiral crystals *Proc. R. Soc.* A **459** 1261–92
[22] Wolfram S 1996 *The Mathematica Book* (Cambridge: Cambridge University Press)
[23] Abramowitz M and Stegun I A 1972 *Handbook of Mathematical Functions* (Washington, DC: National Bureau of Standards)
[24] Tricker R A R 1970 *Introduction to Meteorological Optics* (New York: Elsevier)
[25] van de Hulst H C 1981 *Light Scattering by Small Particles* (New York: Dover)
[26] Nussenzveig H M 1992 *Diffraction Effects in Semiclassical Scattering* (Cambridge: Cambridge University Press)
[27] Ford K W and Wheeler J A 1959 Semiclassical description of scattering *Ann. Phys.* **7** 259–86
[28] Berry M V and Mount K E 1972 Semiclassical approximations in wave mechanics *Rep. Prog. Phys.* **35** 315–97
[29] Deschamps G A 1971 Gaussian beam as a bundle of complex rays *Electron. Lett.* **7** 684–5
[30] Berry M V, Bhandari R and Klein S 1999 Black plastic sandwiches demonstrating biaxial optical anisotropy *Eur. J. Phys.* **20** 1–14